Research Square

Preprints are preliminary reports that have not undergone peer review.
They should not be considered conclusive, used to inform clinical practice,
or referenced by the media as validated information.

Multidisciplinary Screening of a 178 kN Class Geared Turbofan with Explicit Mission Auditing and Independent Uncertainty Checks

Taha Yasin AKYILDIZ

tya346@gmail.com

Republic of Turkey Ministry of National Education: Turkiye Cumhuriyeti Milli Egitim Bakanligi
https://orcid.org/0000-0002-5321-1368

Research Article

Keywords: geared turbofan, component matching, uncertainty quantification, hot-section cooling, rotordynamics, active magnetic bearing

Posted Date: November 4th, 2026

DOI: https://doi.org/10.21203/rs.3.rs-11608672/v1

License: This work is licensed under a Creative Commons Attribution 4.0 International License.
Read Full License

Additional Declarations: The authors declare no competing interests.

Multidisciplinary Screening of a 178 kN Class Geared Turbofan with Explicit Mission Auditing and Independent Uncertainty Checks

Taha Yasin Akyıldız, PhD

Sarıçam Guidance and Research Center, Ministry of National Education, Adana, Türkiye

Corresponding author Taha Yasin Akyıldız E-mail tya346@gmail.com

ORCID 0000-0002-5321-1368 Article type Original Paper

Abstract

A computational audit examines cycle matching, hot-section protection, parallel rotor screening, and uncertainty for a 177.93 kN geared turbofan. Constant-property cycle balances, analytic component maps, fixed nozzle areas, a three-node transient thermal network, and a conceptual flexible rotor are used. The selected static point has bypass ratio 12.99, overall pressure ratio 45.18, turbine-inlet temperature 1450 K, and thrust-specific fuel consumption 22.67 kg/(kN h). Reproduction exposes an inherited input in the historical Monte Carlo loop and thermal boundary conditions disconnected from matched mission states. An independent 10000-draw static holdout records six temperature exceedances and 414 nozzle-pressure-margin failures, with 95% Wilson intervals of 0.028-0.131% and 3.767-4.548%. Matched thermal coupling raises the original-cooling peak to 1255 K. One revised global law reduces the nominal peak to 1230 K at 11.50% takeoff cooling. A separate 5000-draw full-mission thermal analysis with that law frozen records 210 exceedances of 1250 K (4.20%; 95% interval 3.68-4.79%) and no numerical failures. Thus nominal recovery does not establish a mission thermal reliability claim. All eight phases converge, remain within analytic coordinate bounds, and satisfy nozzle forward-flow checks. Compressor surge margins remain undefined because instability boundaries are unavailable. Rotor response is screened over an independent speed sweep, not a recovered mission shaft-speed trajectory. The results support a reproducible conditional screening audit; full compressor operability and hardware performance remain unvalidated. The cooling result remains conditional because detailed cooling-system pressure losses and film-cooling aerodynamics are not resolved.

Keywords: geared turbofan; component matching; uncertainty quantification; hot-section cooling; rotordynamics; active magnetic bearing

1 Introduction

A fixed thrust requirement can conceal an inadmissible internal engine state. An apparently favorable fuel-consumption estimate is insufficient when turbine work leaves inadequate exhaust pressure, cooling is inconsistent with the operating condition, or a solution lies beyond a component instability boundary. A useful preliminary-design workflow must expose these failures before interpreting performance differences.

Recent adaptive-cycle literature emphasizes performance design, measured component matching, variable geometry, and control [1, 2, 3, 4]. The experimental component information used by Cheng et al. is a stronger basis than analytic characteristic functions alone. Integrated thermal-management and transient energy models likewise show why heat transfer and internal mass redistribution belong inside the propulsion calculation [5, 6, 7]. These publications establish the broader coupling problem; they do not supply independent validation data for the KAM-40R cycle or its component characteristics.

Component matching and map scaling are established methods. NASA modeling guidance, pyCycle, and GTlab provide documented approaches to assembling engine simulations [8, 9, 10]. Their existence shifts the research question from whether matching can be performed to whether a particular screening result survives an explicit audit. Coordinate bounds limit mathematical extrapolation, whereas surge and rotating stall depend on additional compressor and system physics [11]. A bounded analytic map is therefore insufficient evidence of stable operation.

Hot-section protection and rotor control impose separate evidence requirements. Thermal-barrier coatings reduce metal heat exposure, but durability also depends on oxidation, evolving interfaces, stress, and coating failure [12, 13, 14]. Flexible rotors require distributed inertia and gyroscopic coupling [15]. Magnetic support adds actuator and control

constraints; recent work addresses vibration suppression and state estimation rather than treating magnetic assistance as an ideal bearing replacement [16, 17, 18].

KAM-40R is a computational case for a 177.93 kN geared turbofan. The assessment separates numerical convergence, analytic coordinate-domain checks, nozzle forward flow, and unresolved compressor operability. Thermal boundaries follow the matched mission states, while rotor dynamics remain a parallel subsystem screening calculation. Independent static and mission thermal samples expose uncertainty around the selected point and its frozen cooling law. The contribution is a reproducible multidisciplinary audit that retains failures and defines the remaining validation requirements.

2 Computational methods

2.1 Architecture and assumptions

Figure 1 shows a geared fan, two-spool core, and separate bypass and core exhaust streams. The high-pressure compressor (HPC) drives the high-pressure turbine (HPT) load; the low-pressure turbine (LPT) supplies fan and low-pressure compressor (LPC) work. Variable stator vanes (VSV) and a variable bleed valve (VBV) are represented by schedules. HPC cooling air bypasses the combustor and returns before the HPT; 1% customer bleed leaves the cycle. Active magnetic bearing (AMB) assistance supplements mechanical rotor support. The schematic defines topology, not manufacturing geometry.

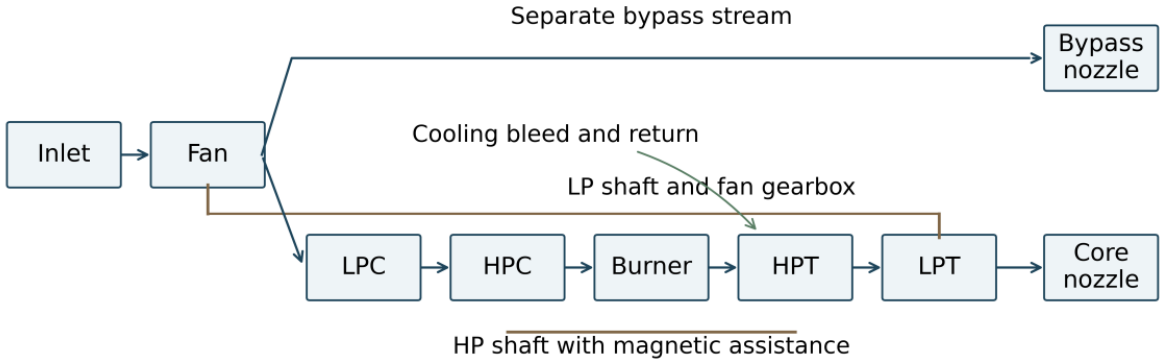


Fig. 1 Two-stream screening architecture with cooling return and separate shaft systems

Table 1 lists the frozen static design and its principal assumptions. The 2.64 m fan diameter follows an annulus mass-flow proxy with hub-to-tip ratio 0.30 and axial capture speed 155 m/s. Detailed inlet and nacelle aerodynamic design are unavailable. Constant specific heats and heat-capacity ratios approximate the working fluids. There is no separate auxiliary power extraction term in the selected Step 9B cycle.

Table 1 Selected static point and assumption provenance

Quantity	Value	Source or rationale
Static thrust	177.93 kN	Prescribed 40,000 lbf class target
BPR / OPR	12.99 / 45.18	Reproduced bounded search
Fan / LPC / HPC pressure ratio	1.207 / 1.152 / 32.49	Search; HPC ratio derived from OPR
Combustor outlet temperature	1450 K	Selected design; not mixed HPT inlet
Design cooling / customer bleed	7.99% / 1.00%	Cooling search / author assumption
TBC thickness / conductivity	0.73 mm / 1.5 W/(m K)	Thermal screening variables

Quantity	Value	Source or rationale
Fan diameter	2.64 m	Flow proxy; not installation validation
Gear / shaft efficiency	0.985 / 0.990	Author assumptions
Burner pressure ratio / mixing loss	0.96 / 1.5%	Fixed author assumptions
Component efficiencies	0.92 fan; 0.91 LPC/HPC; 0.915 HPT; 0.925 LPT	Fixed nominal author assumptions
cp air / hot gas; gamma	1004 / 1150 J/(kg K); 1.40 / 1.33	Constant-property approximation
Fuel heating value / burner efficiency	43 MJ/kg / 0.99	Model assumptions
Nozzle velocity-energy factor	0.985	Assumed effective velocity coefficient squared

2.2 Cycle and component matching

Compressor total-temperature rise and combustor fuel-air ratio follow Eqs. (1)-(2). Subscripts i and o indicate inlet and outlet; c and t identify air and hot-gas properties. Tt3 is HPC exit total temperature and Tt4 is combustor outlet total temperature. The symbols πc, ηc, ηb, and LHV denote compressor pressure ratio, compressor efficiency, burner efficiency, and fuel lower heating value. Cooling-air enthalpy is mixed before HPT work is calculated, so combustor outlet and mixed HPT inlet temperatures differ. The model uses cp,c = 1004 J/(kg K), cp,t = 1150 J/(kg K), γc = 1.40, γt = 1.33, and R = 287.05 J/(kg K); LHV = 43 MJ/kg and ηb = 0.99. Constant-property error is model-form uncertainty and is not sampled in either Monte Carlo set.

$$T_{t,o} = T_{t,i}\left[1 + \frac{\pi_c^{\frac{\gamma_c - 1}{\gamma_c}} - 1}{\eta_c}\right] \quad (1)$$

$$f = \frac{cp_t T_{t4} - cp_c T_{t3}}{\eta_b LHV - cp_t T_{t4}} \quad (2)$$

A one-stage fan, two-stage LPC, 12-stage HPC, three-stage HPT, and three-stage LPT remain provisional architecture choices. Earlier mean-line checks used loading limits of 0.45 for the LPC, 0.48 for the HPC, 1.25 for the HPT, and 1.10 for the LPT, with a 1.35 HPC tip-relative-Mach limit. These stage screens are not embedded in the final seven-variable search objective. Detailed stage geometry has not been regenerated for every final operating condition, so the stage counts cannot establish final blade feasibility.

The fan, LPC, and HPC use analytic normalized corrected-flow functions. Equation (3) defines Wc from mass flow ṁ, total temperature Tt, and total pressure Pt, with Tref = 288.15 K and Pref = 101325 Pa. Equations (4)-(6) give the EM-line family: e is an operating-line coordinate, n is a normalized analytic map-speed coordinate, and subscript d denotes the design anchor. The fan and LPC share nL; the HPC uses nH. No validated conversion from these coordinates to phase-by-phase physical shaft rpm is available. The model therefore does not provide a mechanical mission-speed trajectory.

$$W_c = \frac{\dot{m}\sqrt{\frac{T_t}{T_{ref}}}}{\frac{P_t}{P_{ref}}} \quad (3)$$

$$\frac{W_c}{W_{c,d}} = max[0.04, 0.24 + 0.76 n^{p_w} + s(0.62 + 0.38\, n)e] \quad (4)$$

$$\pi = max\{1.003, 1 + (\pi_d - 1)n^{p_\pi} max[0.18, 1 - ae - 0.10e^2]\} \quad (5)$$

$$\eta = clip[\eta_d - 0.035(n-1)^2 - 0.060e^2, 0.66, 0.94] \quad (6)$$

The coefficients (s, a, pπ, pw) are (0.50, 0.15, 1.45, 1.05) for the fan, (0.44, 0.18, 1.42, 1.02) for the LPC, and (0.40, 0.12, 1.20, 0.95) for the HPC. Here s sets flow-line spacing, a sets pressure-line slope, and pπ and pw are speed exponents; η is efficiency. Turbine flow compatibility uses the design-normalized function $\sqrt{[(1 - \pi^{-a})/(1 - \pi_d^{-a})]}$ (0.90 + 0.10n), with a = 0.16 for the HPT and 0.05 for the LPT. All map coefficients are author assumptions, not measured characteristics or validated stability envelopes.

One static sizing calculation fixes core and bypass nozzle areas and the map-flow anchors. Each mission phase solves six unknowns: nL, nH, combustor outlet temperature, and three EM coordinates. The six residuals cover HPC corrected flow, HPT compatibility, LPT compatibility, core and bypass nozzle continuity, and installed thrust. Shaft work is enforced within the state calculation and checked again as an algebraic identity. Sixteen initial guesses are used per phase: four speed scalings combined with four EM triplets. Bounded least squares uses at most 9000 function evaluations per start and ftol = xtol = gtol = 10^(−11). The thrust residual receives weight 12; acceptance uses unweighted residuals.

The numerical domains are $0.12 \le nL \le 1.24$, $0.12 \le nH \le 1.26$, $-1 \le e \le 1$, and $700\ K \le TIT \le TITd+110\ K$. Numerical convergence requires an unweighted residual norm below 10^(−6) and normalized mass and shaft-work errors below 10^(−6). Coordinate-domain admission additionally requires all variables within their declared analytic bounds. These computational checks do not determine compressor stability.

Convergent nozzle choking is evaluated at Pt/pa = [(γ + 1)/2]^(γ/(γ − 1)). Exit pressure pe equals ambient pressure pa below choking and critical pressure above choking. Equation (7) sums gross momentum and pressure thrust Fg using exit velocity Ve and area Ae; net thrust subtracts inlet momentum ṁ0V0. The mass-flow function is ideal isentropic; the 0.985 factor modifies velocity energy. Correcting the original mismatch between choked continuity and fully expanded velocity changes the largest phase thrust by 0.00130%. Nozzle forward-flow admission requires Pt > pa in both streams; nozzle choking does not define a compressor choke boundary.

$$F_g = \dot{m}V_e + (p_e - p_a)A_e; F_{net} = \Sigma F_g - \dot{m}_0 V_0 \quad (7)$$

A compressor surge margin would require validated surge-line pressure ratio πs and corrected flow Wc,s at a specified speed, for example SM = 100[(Wc,op/Wc,s)(πs/πop)−1], where op identifies the operating point. The analytic functions contain no compressor surge or choke line. Fan, LPC, and HPC surge margins are ND, meaning not defined. Four evidence levels are kept separate: numerical convergence; coordinate-domain admission; nozzle forward-flow admission; and full physical compressor operability. The first three can be checked here; the fourth remains unevaluated. The coordinate e = −1 is not a synthetic surge boundary.

2.3 Design selection and stopping record

Seven continuous variables and their bounds are listed in Table 2. Differential evolution minimizes nominal static thrust-specific fuel consumption (TSFC) plus explicitly weighted penalties [19]. Let Π denote P5/pa, Tm the steady metal hot-face temperature, D the fan diameter proxy, c the cooling fraction, and t the coating thickness in millimetres. The objective adds 2200(1.35−Π)²+120 if Π<1.35, 0.20(Tm−1200)²+120 if Tm>1200, and 100(D−2.65)²+10 if D>2.65. Further terms are 15 max(0,c−0.08)/0.01 and 2 max(0,t−0.65). Invalid cycle evaluations receive 106. The penalty weights are heuristic scalar screening weights.

Table 2 Continuous design-search bounds

Variable	Lower	Upper
BPR	10.5	13.0
OPR	38	50
FPR	1.15	1.32

Variable	Lower	Upper
LPC pressure ratio	1.15	1.55
TIT (K)	1450	1550
Design cooling fraction	0.060	0.085
TBC thickness (mm)	0.45	0.75

The reproduced SciPy 1.17.0 search uses seed 101, best1bin strategy, Latin-hypercube initialization, 126 population members (18 per variable), mutation 0.5-1.0, recombination 0.7, immediate updating, and local polishing. It allows 110 generations and relative population-energy tolerance 10^(−7) with zero absolute tolerance. One independently initialized run performs 14154 objective evaluations and stops at the generation limit with success = false. The returned point is a selected nominally feasible candidate. No convergence-to-global-optimum claim is made. The design search is not rerun in this revision.

Stage counts are fixed assumptions, not discrete search variables. Monte Carlo is performed after the deterministic search and is not an inner optimization constraint. The retained 3000 draws constitute a development check. Separate nominal tests require $\Pi \geq 1.35$ and a steady thermal margin of at least 40 K; uncertainty events are metal temperature above 1250 K and Π below 1.12. These static conditions do not automatically impose a 1.12 margin on every low-power mission phase.

2.4 Mission definition and common demand

Table 3 defines all eight phases of the six-hour profile. Two engines are assumed. Per-engine demand is taken from the archived conventional surrogate and applied unchanged to the candidate; aircraft demand is twice that value. No aircraft type, drag polar, changing aircraft weight, or flight-path dynamics is specified. Consequently the common demand is an imposed profile rather than a calculated aircraft thrust requirement.

Table 3 Complete imposed mission and candidate installation allowance

Phase	h	Altitude m	Mach	Aircraft thrust kN	Candidate factor
Taxi	0.20	0	0.00	65.67	0.9812
Takeoff	0.10	0	0.15	309.51	0.9776
Climb	0.35	6000	0.55	109.43	0.9680
Cruise A	2.20	11000	0.78	41.39	0.9625
Cruise B	2.20	11000	0.78	39.83	0.9625
Descent	0.45	5000	0.45	42.61	0.9704
Approach	0.20	0	0.20	77.76	0.9764
Reserve	0.30	3000	0.35	75.53	0.9728

Candidate installed thrust equals $a(M,D_{fan})F_{net}$, where $a = \max[0.935, 0.985 - 0.024M - 0.004 \max(D_{fan} - 2.4, 0)/0.25]$. This empirical allowance is an author assumption. It differs from the reference nacelle-drag treatment and is not an aircraft integration calculation. Mission fuel is $2\Sigma \dot{m}_{f,i} \Delta t_i$; all source phase durations and both engine counts are preserved.

Table 4 specifies the conventional reference. Corrected core-flow scaling follows inlet total pressure and temperature. Part-power gross thrust is multiplied by $\max(0.08, \theta^{1.05})$ and fuel by $0.08 + 0.92\theta^{0.82}$, where θ is the imposed phase throttle: 0.20, 1.00, 0.82, 0.58, 0.56, 0.30, 0.28, and 0.40. Installed thrust subtracts $qC_d\pi D_{fan}^2/4$, where q is dynamic pressure and $C_d = 0.032$. Reference diameter uses capture speed 165 m/s and hub-to-tip ratio 0.32. These surrogate laws do not establish fixed-area component matching at part power.

Table 4 Archived conventional surrogate inputs

Input	Value	Meaning
SLS thrust / BPR	177.93 kN / 5.9	Same static class; assigned bypass ratio
OPR / FPR / TIT	30.8 / 1.55 / 1650 K	Assigned cycle inputs
Fan / core-compressor efficiency	0.91 / 0.90	Assigned component efficiencies
Turbine / gearbox efficiency	0.92 / 1.00	Common turbine value; direct-drive reference
Bleed / auxiliary power	3.5% / 250 kW	Reference cycle allowances

Input	Value	Meaning
Inlet / burner pressure recovery	0.995 / 0.96	Fixed scalar losses
Burner / mechanical efficiency	0.995 / 0.992	Reference assumptions
Nozzle / heating value	0.985 / 43 MJ/kg	Velocity-energy factor; same heating value

2.5 Thermal coupling and nominal cooling revision

The three thermal nodes are coating hot face, metal hot face, and metal core. Gas convection and radiation feed the coating; conduction links coating and metal; internal convection removes heat to the HPC cooling air. The network uses Ahot = 0.010 m², Acool = 0.0045 m², gas coefficient 1800 W/(m² K), reference cooling coefficient 1200 W/(m² K), emissivity 0.55, metal conductivity 18 W/(m K), and metal conduction path 3 mm. Heat capacities and generic material inputs are given in Online Resource 1. Literature motivates the model structure but does not calibrate these author-selected coefficients [20].

The original thermal branch prescribed gas and cooling temperatures from throttle and altitude separately from mission matching. Revised coupling supplies each phase mixed HPT inlet temperature, HPC exit temperature, and solved cooling fraction. Phase states remain piecewise steady; temperature dynamics use Radau with relative and absolute tolerances 10^{-7} from an initial 300 K condition. Cooling convection scales as 1200 (c/0.045)^0.75 W/(m² K). The cycle does not simulate acceleration, film-cooling holes, or conjugate heat transfer.

The original schedule is c0= 0.030+(cd−0.030)p^0.8, with p = clip[(TIT−800)/(TITd−800),0,1.15], cd the design cooling fraction, and TITd the design combustor outlet temperature. Equation (8) adds cooling above design thermal power. A bracketed scalar development search over k = 0-0.35 targets 1230 K takeoff equilibrium, then rounds k upward to 0.194. The full transient mission is replayed with no change to maps, nozzle areas, or phase-specific controls. The assumed cooling cap is 12%; a 1225 K target is not reachable within that cap. The final k = 0.194 law is frozen before mission thermal sampling.

$$c = clip[c_0 + 0.194\, max(0, p-1), 0.030, 0.120] \quad (8)$$

Stress combines a centrifugal proxy at the assumed 11000 rpm structural reference with temperature-gradient stress. Actual mission mechanical speed is not recovered from the shared normalized map coordinates. Generic strain-life and creep surrogates provide a cumulative damage indicator. Linear accumulation follows a Miner-type accounting framework [21]; material-specific rupture evidence is required for a usable life assessment [22]. Numerical strain-life ceilings and inverse damage are not service-life predictions.

2.6 Parallel rotor and magnetic-assistance screening

The rotor contains eight Euler-Bernoulli beam nodes with four lateral and rotational degrees of freedom per node. Seven shaft diameters range from 80 to 95 mm over a 1.80 m axis. Three grouped HPC/HPT disks supply masses 38, 52, and 44 kg and assigned diametral/polar inertia. Mechanical supports remain at the end nodes; two AMB stations add scheduled stiffness and damping. The mass, stiffness, damping, and disk gyroscopic matrices and imbalance inputs are supplied in Online Resource 1. Equation (9) uses generalized coordinates q, mass M, damping C including scheduled magnetic assistance, stiffness K, added AMB stiffness KAMB, disk gyroscopic matrix G, physical angular speed Ω, and harmonic imbalance force Funbalance. Since nH is not converted to validated mission shaft rpm, the rotor uses an independent speed sweep. The 11000 rpm value is a structural screening reference; solved mission states do not drive the rotor calculation.

$$M\,\ddot{q} + (C + \Omega G)\,\dot{q} + (K + K_{AMB})q = F_{unbalance} \quad (9)$$

The reproduced schedule gives kAMB = 2.0 MN/m and cAMB= [12+18s0.7] kN s/m, where s = clip(rpm/11000,0,1.30). Differential evolution tunes five schedule parameters with seed 26, 60 population members, and 45 allowed generations

against an 80-point speed grid; response is checked on 156 points from 500 to 16000 rpm. The 500 μm backup clearance and 20 kN radial-force ceiling are author screening assumptions. Calculated force is linear; electromagnetic sizing, saturation, amplifier current and voltage limits, sensor delay, bandwidth, heating, and nonlinear touchdown contact are not modeled. The 18.65 kN arithmetic difference is not demonstrated actuator reserve.

2.7 Public transient consistency check

NASA C-MAPSS40k supplies an external reference for the architecture of a commercial 40000 lbf class engine and controller [23, 24]. Approximate graph readings represent the documented 2000 ft, Mach 0.25, 50%-deteriorated idle-to-full-power transient. Fourteen time samples are retained. Six alternating transient points fit generalized rise curves and the remaining six transient points assess interpolation; two earlier idle samples are excluded from the holdout metric. Core speed uses an additional overshoot term. The fit has separate parameters for each trace.

Errors are normalized by fixed thrust, fan-speed, and core-speed spans of 22000 lbf, 1600 rpm, and 1850 rpm. The benchmark supports limited consistency of the reduced controller/transient representation, not direct validation of the KAM-40R compressor and turbine maps. Withheld samples come from the same digitized transient, not independent engine operating conditions. Cycle prediction, compressor stability, and aircraft mission accuracy are not validated by this fit.

2.8 Static development and independent uncertainty sets

The nominal parameter vector is frozen before sampling. Each draw resizes core flow to fixed thrust; hardware nozzle areas are not held fixed. The retained development seed is 917; the independent 10000-draw static holdout uses seed 20261003 without design retuning. FPR, OPR, and LPC ratio have independent relative normal standard deviations of 1%, 2%, and 1.5%; TIT has 15 K standard deviation. Cooling has 0.0035 absolute-fraction standard deviation and is clipped to 0.055-0.095. Component efficiencies have standard deviation 0.008, with the explicit clips retained in the executable package. Coating thickness and conductivity have standard deviations 0.04 mm and 0.12 W/(m K), clipped to 0.50-0.85 mm and 1.1-1.9 W/(m K). Gas convection varies by 7%; the cooling multiplier varies by 8% and is clipped to 0.75-1.25. Inputs are assumed independent; these are uncertainty assumptions, not experimentally measured distributions.

The original Step 9B Monte Carlo loop referred to a notebook-global BPR of 12.9999568 from Step 8D rather than the selected 12.9906323. An explicit historical replay recovers the published 131/3000 pressure failures. The corrected development replay and holdout both use the frozen selected BPR. Every requested draw is recorded; invalid states and thermal root failures are counted separately without replacement sampling. No numerical failures occur in these sets. A root is accepted only when converged and the largest thermal balance error is below 10^(−5) W.

Event frequencies k/N receive two-sided 95% Wilson intervals [25, 26], conditional on the assumed model and input law. These sampling intervals exclude measured-map uncertainty, unmodeled material degradation, correlated inputs, controller uncertainty, constant-property error, and aircraft installation uncertainty. Historical 3000-draw, corrected development 3000-draw, and independent 10000-draw static sets remain separate from the mission analysis below. Static draws resize the engine to fixed thrust and do not test fixed-hardware mission reliability. Pearson correlations are linear associations, not variance-based global sensitivity indices [27].

A large language model assisted code prototyping, auditing, and manuscript drafting; the author retains responsibility.

2.9 Independent-sample full-mission thermal uncertainty

A new deterministic seed, 20261017, generates 5000 independent Monte Carlo samples for full-mission thermal integration after freezing k = 0.194 and the matched eight-phase states. Each realization replays all six hours from 300 K, carrying the three temperatures continuously across phase boundaries. Radau integration uses an analytic

Jacobian and 10^(−7) relative and absolute tolerances. Maximum metal hot-face temperature is checked at solver nodes, phase endpoints, and resolved interior stationary maxima; its time and phase are saved. Failed draws are retained and counted separately, with no replacement sampling.

Four thermal input laws are reused from the static analysis: coating thickness is normal about 0.7302927 mm with standard deviation 0.04 mm, clipped to 0.50-0.85 mm; coating conductivity is normal about 1.5 W/(m K) with standard deviation 0.12, clipped to 1.1-1.9; gas convection is normal about 1800 W/(m² K) with standard deviation 126; and the cooling-convection multiplier is normal about 1.0 with standard deviation 0.08, clipped to 0.75-1.25. One independent realization of each parameter is held throughout a complete mission. Thickness affects coating resistance and heat capacity. These distributions remain author modeling assumptions.

The event is Tmax > 1250 K. TIT, cooling fractions, map coefficients, nozzle areas, phase demand, and controller settings are unchanged; gas and cooling-air temperatures remain the nominal matched values. TIT or cooling-fraction perturbations are omitted because consistent propagation would require additional cycle rematching. This is a conditional mission thermal analysis, not controller validation or full engine reliability. No mission probability acceptance limit was set before this run, and no cooling-law retuning follows an unfavorable result.

3 Results

3.1 Reproduced selected static point

Table 5 gives the nominal static outputs. The reproduced search returns the exact archived design coordinates and scalar outputs, despite stopping at its iteration limit. The selected point retains a 1.354 core-nozzle pressure ratio and 50.1 K steady metal-temperature margin. The large fan remains an installation risk. These values represent one selected cycle under its stated approximations, rather than a demonstrated optimum or a measured engine.

Table 5 Nominal static cycle outputs

Metric	Result
Static TSFC	22.67 kg/(kN h)
Core nozzle total pressure / ambient	1.354
Mixed HPT inlet temperature	1398.5 K
HPC exit temperature	917.1 K
Steady metal hot face	1199.9 K
Steady temperature margin	50.1 K
Fan diameter proxy	2.64 m

3.2 Independent static holdout

Figure 2 and Table 6 distinguish historical, corrected development, and independent holdout calculations. Correcting the inherited BPR reduces development pressure-margin failures from 131 to 126 without changing the three thermal events. The holdout gives six thermal events and 414 pressure-margin events. Its 95% upper bounds, 0.131% and 4.548%, lie below the declared 2% and 5% static screening limits. This supports the chosen nominal margins under the assumed uncertainty law; it provides no certification reliability probability.

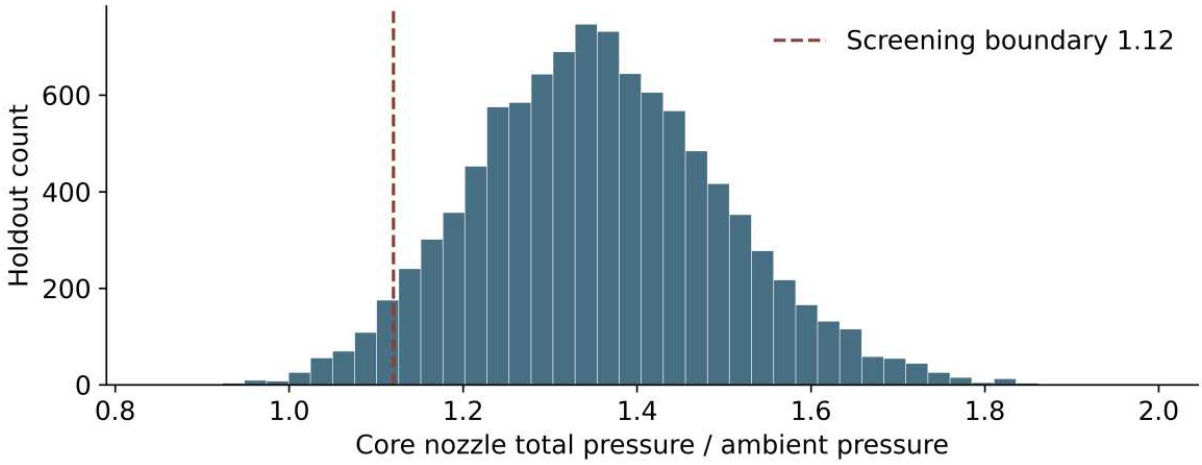


Fig. 2 Independent 10000-draw static core-nozzle pressure distribution with the 1.12 screening boundary

Table 6 Event counts and two-sided 95 percent Wilson intervals

Set and event	k / N	Estimate %	95% interval %
Historical thermal	3 / 3000	0.100	0.034-0.294
Historical pressure	131 / 3000	4.367	3.692-5.158
Corrected development thermal	3 / 3000	0.100	0.034-0.294
Corrected development pressure	126 / 3000	4.200	3.539-4.978
Independent holdout thermal	6 / 10000	0.060	0.028-0.131
Independent holdout pressure	414 / 10000	4.140	3.767-4.548

The holdout fifth-percentile pressure ratio is 1.132; its 95th-percentile metal temperature and static TSFC are 1224.3 K and 23.34 kg/(kN h). Figure 3 shows the temperature distribution. TIT has the largest absolute linear correlation with TSFC (0.672); TIT and the cooling multiplier lead metal-temperature correlations (0.565 and −0.544). FPR leads pressure-ratio correlation (−0.730). The earlier claim that HPT efficiency was the largest TSFC driver does not apply to this final-point holdout.

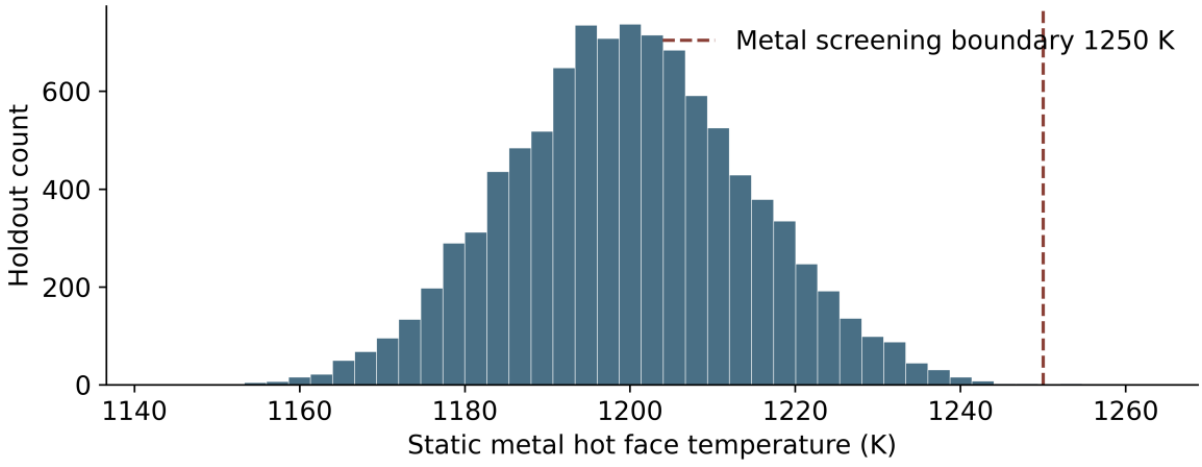


Fig. 3 Independent static holdout metal-temperature distribution with the 1250 K screening boundary

3.3 Mission thermal coupling and damage indicator

Figure 4 compares the original throttle-driven branch, matched-state coupling, and revised common cooling law. Table 7 shows why the original 1202.5 K peak could not establish mission thermal compliance: matched states

instead yield 1255.0 K and cross the 1250 K screen. The revised global law reduces the nominal transient peak to 1229.96 K, a 20.0 K margin. Takeoff combustor outlet temperature is 1552.5 K and cooling is 11.50% of core flow; nominal design TIT remains 1450 K. Uncertainty around this nominal recovery is evaluated separately in Sect. 3.7.

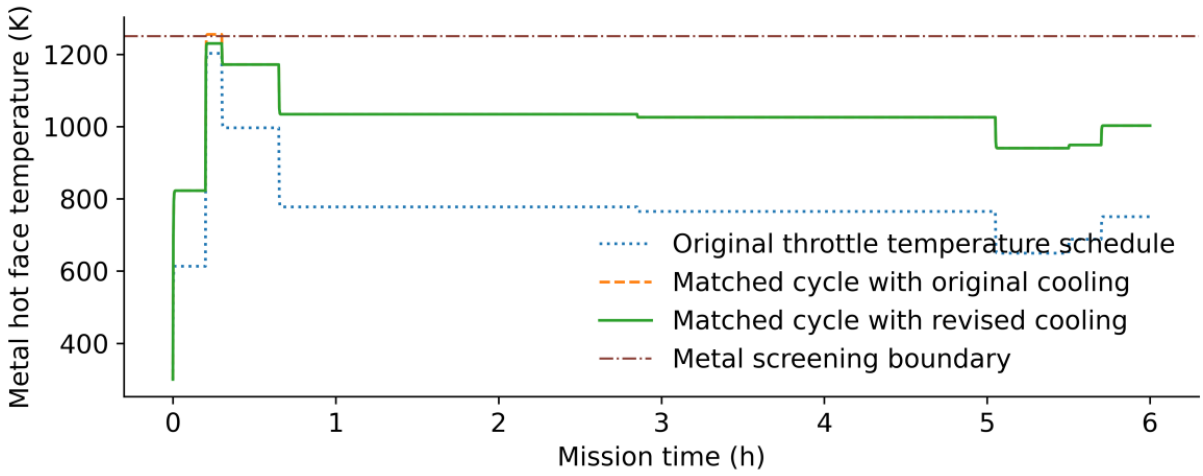


Fig. 4 Nominal thermal histories for the disconnected boundary schedule and two matched-state cooling scenarios

Table 7 Thermal screening before and after mission coupling

Metric	Original schedule	Matched original cooling	Revised common cooling
Peak metal hot face K	1202.5	1255.0	1230.0
Margin to 1250 K	47.5	−5.0	20.0
Peak metal gradient K	39.4	41.2	43.9
Peak combined stress MPa	376.8	377.1	378.1
Minimum yield-margin proxy	1.41	1.38	1.38
Cumulative damage per profile	≈4.9×10^(−6)	≈3.0×10^(−5)	≈2.6×10^(−5)

The revised scenario retains a generic cumulative damage indicator. The strain-life law reaches its imposed 108-cycle numerical ceiling, which censors that parameter. Inverse generic Miner damage is not interpreted as component service life. Oxidation, bond-coat evolution, TBC spallation, creep-fatigue interaction, local film-cooling geometry, conjugate heat transfer, and material-specific rupture behavior remain unresolved.

3.4 Conditional rotor-dynamic screening

The reproduced flexible-rotor result retains a 109.4 µm peak displacement at 2100 rpm and 390.6 µm clearance to the assumed backup boundary. Figure 5 shows the ordered modal frequencies; simple frequency sorting does not provide complete mode-branch tracking. Table 8 separates computed force demand from the assumed actuator ceiling. The 43.3% lower critical-speed separation is evaluated relative to 11000 rpm. No upper synchronous crossing appears within the scanned range; this does not establish a quantified upper separation beyond 16000 rpm. Future modal-assurance-criterion tracking could follow mode branches through crossings; it has not been performed. This is parallel subsystem screening, not a mission-driven rotor trajectory.

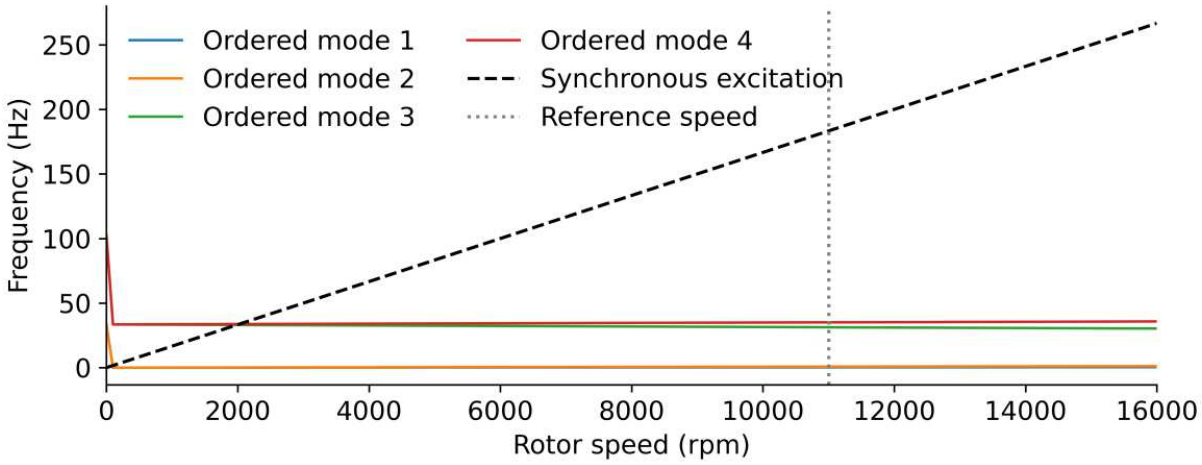


Fig. 5 Frequency-sorted modal curves from an independent rotor speed sweep with idealized magnetic assistance

Table 8 Rotor response with explicit actuator-model limits

Metric	Result	Interpretation
Peak displacement / backup margin	109.4 / 390.6 μm	Linear harmonic response / assumed clearance
Maximum calculated radial AMB force	1.35 kN	Linear force demand
Assumed radial-force ceiling	20 kN	Author assumption; no electromagnetic sizing
Difference to assumed ceiling	18.65 kN	Arithmetic only; not actuator reserve
Lower synchronous critical separation	43.3%	Relative to fixed 11000 rpm reference
Minimum modal damping at reference speed	0.203	Idealized support and controller model

3.5 Public transient fit

Table 9 reproduces the public-trace consistency metrics. The thrust and fan-speed interpolation errors are small relative to their selected spans, while core speed shows a larger discrepancy. These errors measure a separately fitted reduced transient representation. They establish neither steady-cycle prediction accuracy nor validation of KAM-40R compressor or turbine maps.

Table 9 Approximate NASA transient fit on six withheld transient samples

Quantity	Error as percent of declared span
Net thrust RMSE / MAE	1.06 / 0.63
Fan speed RMSE	0.27
Core speed RMSE	7.23

3.6 Eight-phase coordinate-bounded mission matching

Figure 6 and Table 10 show the revised-cooling mission audit with fixed map anchors and nozzle areas. All eight phases meet numerical convergence, coordinate-domain admission, and nozzle forward-flow admission. The largest unweighted residual norm is $1.73\times10^{(-14)}$; normalized total-mass and both shaft-work errors remain below $10^{(-15)}$. These checks demonstrate internal numerical consistency. Compressor surge margins remain ND, so full physical compressor operability is unevaluated.

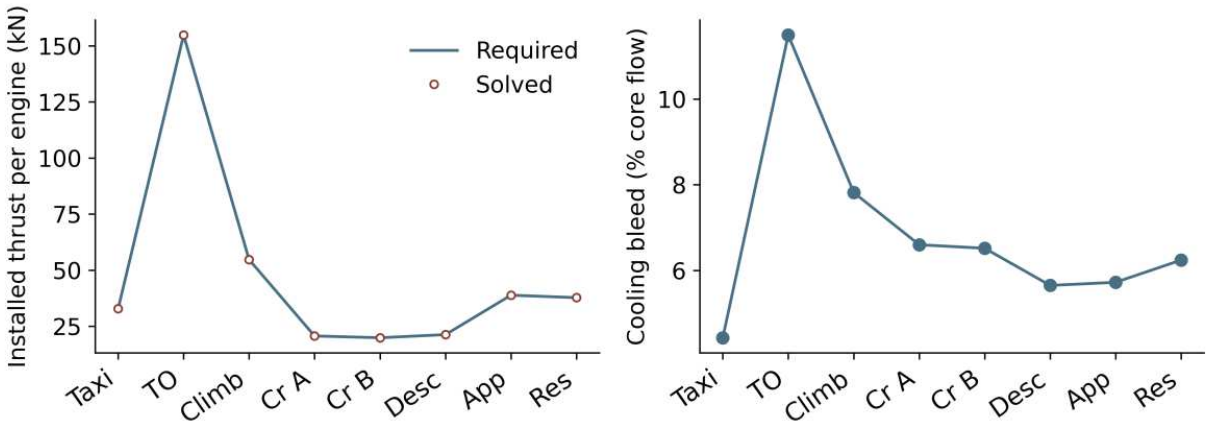


Fig. 6 Imposed and numerically matched per-engine thrust with the frozen cooling schedule for eight coordinate-bounded phases

Table 10 Mission numerical and coordinate checks; compressor operability remains unevaluated

Phase	Fan SM	LPC SM	HPC SM	Domain	Core / bypass	Residual norm
Taxi	ND	ND	ND	Within bounds	U / U	6.0×10^(−15)
Takeoff	ND	ND	ND	Within bounds	U / U	3.0×10^(−15)
Climb	ND	ND	ND	Within bounds	U / U	1.5×10^(−15)
Cruise A	ND	ND	ND	Within bounds	C / U	6.3×10^(−16)
Cruise B	ND	ND	ND	Within bounds	U / U	1.9×10^(−15)
Descent	ND	ND	ND	Within bounds	U / U	2.6×10^(−15)
Approach	ND	ND	ND	Within bounds	U / U	1.7×10^(−14)
Reserve	ND	ND	ND	Within bounds	U / U	6.8×10^(−15)

ND means no surge line is defined; U and C denote unchoked and choked nozzles with forward flow. All listed mass, shaft, and nozzle continuity checks pass the declared 10^(−6) audit tolerances; the full values, EM coordinates, pressure ratios, and normalized speeds are in Online Resource 1. The minimum core pressure ratio is 1.0227 at taxi. Taxi and approach fall below 1.12, which is the static uncertainty boundary rather than the original mission forward-flow criterion. A uniform 1.12 mission-margin requirement would reject those two phases.

Supplementary Fig. S1 retains a model-internal fuel comparison under a common imposed thrust-demand profile. Candidate fuel is 16.824 t for two engines and the archived reference gives 26.547 t, a 36.63% arithmetic difference. Common demand corrects a historical comparison inconsistency but does not establish aircraft equivalence. Candidate fixed-area matching and reference throttle-surrogate part-power behavior have different fidelity, component assumptions, installation treatment, and operability evidence. Neither model provides validated aircraft-level predictions. Drag polar, changing mass, full flight-path dynamics, nacelle aerodynamics, and propulsion-airframe coupling are not solved. The difference cannot be attributed to engine architecture alone.

The global cooling revision changes takeoff TIT and cooling convection but leaves calculated fuel essentially unchanged. In this lumped constant-property model, cooling is returned before the HPT, the mixing-pressure loss remains fixed, and the matched mixed state and work equations constrain fuel addition. Real cooling-system pressure loss, film-cooling aerodynamics, and additional bleed penalties are not captured by this invariance. It is a model limitation, not a demonstrated ability to increase cooling without fuel cost.

3.7 Independent-sample full-mission thermal uncertainty

Figure 7 and Table 11 report the separate 5000-draw full-mission thermal set. All 5000 simulations complete eight phases; numerical failures are zero. The 1250 K screen is exceeded in 210 draws (4.20%), with a two-sided 95% Wilson interval of 3.678-4.792%. Median Tmax is 1229.9 K, the 95th percentile is 1249.2 K, the 99th percentile is 1256.8 K, and the largest sampled value is 1270.0 K. Every maximum occurs in takeoff. The recorded full-mission peaks agree with a separate takeoff equilibrium-balance check within 0.001 K.

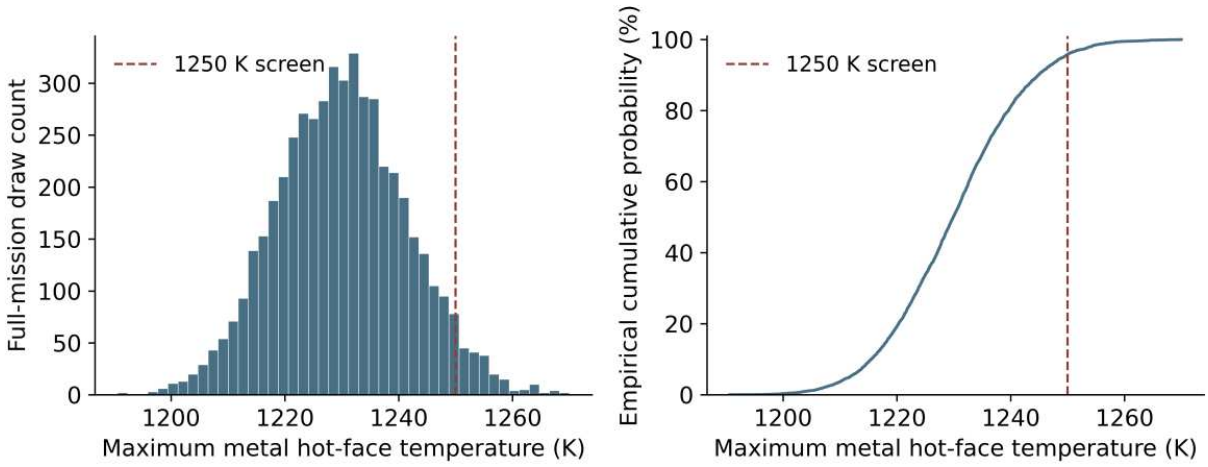


Fig. 7 Full-mission maximum-temperature distribution from 5000 independent samples under the frozen revised cooling law

Table 11 Separate full-mission thermal uncertainty results

Quantity	Result
Requested / successful missions	5000 / 5000
Numerical failures	0
Exceedances of 1250 K / requested missions	210 / 5000
Exceedance frequency	4.20%
Two-sided 95% Wilson interval	3.678-4.792%
Median / 95th percentile Tmax	1229.9 / 1249.2 K
99th percentile / maximum observed Tmax	1256.8 / 1270.0 K
Phase of all maxima	Takeoff
Seed / frozen cooling-law coefficient	20261017 / 0.194

The mission frequency differs from the 0.060% static thermal frequency because the operating boundaries, transient problem, and sampled variables differ. The two rates are not pooled. No mission risk acceptance threshold was declared; these results do not establish acceptable hardware reliability. Nominal cooling recovery leaves a measurable assumed-model upper tail, and the law is not retuned. The cooling multiplier has the largest absolute Pearson association with Tmax (−0.758), followed by coating conductivity (0.459), thickness (−0.326), and gas convection (0.312). Pearson correlations are linear associations, not variance-based global sensitivity indices.

4 Discussion and evidence limits

Reproduction resolves three different questions. The retained Step 10E branch genuinely closes its algebraic phase equations; the earlier failed Step 10 CSV belongs to another calculation and cannot be used to invalidate that final branch. The selected static point and rotor response reproduce exactly. However, the historical uncertainty result uses an inherited BPR and the thermal result uses boundary conditions disconnected from the matched mission. Correcting these issues strengthens traceability and changes the defensible scope of the conclusions.

The static holdout addresses sampling around a frozen static candidate; the new mission set propagates four thermal inputs through a fixed matched trajectory. Neither supplies measured map validity or certification reliability. The mission set does not independently validate the controller or encompass TIT, cooling-schedule, demand, material-degradation, or correlated uncertainty. The bounded design-search stopping record prevents a global-optimality claim. Stage geometry, nacelle aerodynamics, gearbox sizing, auxiliary offtakes, and structural dimensions remain conceptual assumptions.

Full physical compressor operability remains the largest technical gap. Finite EM coordinates and normalized speed bounds restrict mathematical extrapolation but provide no surge or compressor choke distance. Validated

component characteristics and control/transient analysis are required. A separate fit to one digitized C-MAPSS transient cannot bridge that gap.

Matched thermal coupling exposes a hidden temperature violation and the common cooling law restores the nominal screen. The independently sampled mission thermal set nevertheless records 210/5000 exceedances under author-assumed thermal distributions. That evidence supports reporting conditional thermal risk, not hardware acceptance. Material-specific fatigue/creep data, film-cooling geometry, conjugate heat transfer, and coating degradation remain required. The parallel rotor model likewise cannot establish electromagnetic actuator sizing, saturation, achievable damping, or mission shaft-speed response.

5 Conclusions

A reproducible multidisciplinary audit retains a 177.93 kN nominal static point and eight numerically matched mission phases. Numerical convergence, coordinate-domain admission, and nozzle forward-flow admission pass their declared checks. Full physical compressor operability remains unevaluated because validated surge and compressor choke boundaries are absent.

Correcting the inherited Monte Carlo BPR and evaluating an independent 10000-draw static holdout gives six thermal exceedances and 414 pressure-margin failures. Wilson intervals support the declared static screening limits under the assumed distributions. These results do not establish experimentally validated or mission-wide reliability.

Coupling thermal boundaries to matched states raises the original-cooling peak to 1255 K; one common revised law lowers the nominal peak to 1230 K at 11.50% takeoff cooling. With that law frozen, 210/5000 full-mission thermal realizations from independent samples exceed 1250 K (4.20%; 95% interval 3.68-4.79%). Accordingly, nominal thermal compliance and uncertainty-based thermal screening lead to different conclusions. The conditional upper tail is retained without retuning. Generic damage and independently swept rotor response remain subsystem screening indicators. Hardware qualification requires measured maps, material-specific data, actuator physics, and aircraft integration.

Statements and Declarations

Competing Interests. The author declares no financial or non-financial interests directly related to the work.

Funding. No external funding was received for the computational work.

Author Contributions. Taha Yasin Akyıldız: conceptualization, methodology, computational modeling, formal analysis, visualization, writing, and revision.

Data and Code Availability. Online Resource 1 contains executable cycle, mission, thermal, rotor, benchmark, and uncertainty scripts; frozen inputs; every static and mission uncertainty draw; seeds; CSV/JSON summaries; numerical verification; figure sources; change records; and SHA256 hashes. No proprietary maps are reproduced. A public repository accession has not been assigned; no public deposit is claimed.

Use of Generative Tools. OpenAI ChatGPT (GPT-5.6 Sol) was used for initial translation and language editing. The author remains responsible for checking scientific assumptions, results, citations, and approving the submitted version.

Supplementary material

Online Resource 1 Reproducible scripts and frozen inputs, 10000 static holdout rows, 5000 independent full-mission thermal rows, development replays, scenario outputs, numerical audits, figures, source hashes, and remaining validation requirements. Supplementary Fig. S1 shows the model-internal two-engine fuel comparison using non-equivalent surrogate models.

References

[1] Chen, M., Deng, L., Zhang, J., & Tang, H. (2025). Review on the development status and performance design of adaptive cycle engines. Propulsion and Power Research, 14(1), 35-63. https://doi.org/10.1016/j.jppr.2025.02.006

[2] Cheng, R., Zhang, Z., Jia, L., Zhang, X., & Yang, L. (2025). Component matching optimization of high-performance turbofan engine based on experiment test and adaptive performance model to control the average gas temperature. Propulsion and Power Research, 14(1), 1-13. https://doi.org/10.1016/j.jppr.2025.02.001

[3] Wang, Y., Chen, H., Liu, X., & Zhang, H. (2025). Multi-mode acceleration optimization control for adaptive cycle engine based on variable geometry components. Chinese Journal of Aeronautics, 38(9), Article 103460. https://doi.org/10.1016/j.cja.2025.103460

[4] Zhou, X., Chen, W., Huang, J., Liu, J., & Lu, F. (2025). A thrust estimation and control method of an adaptive cycle engine based on improved MFAC algorithm. Chinese Journal of Aeronautics, 38(5), Article 103424. https://doi.org/10.1016/j.cja.2025.103424

[5] Zhuang, L., Xu, G., Dong, B., Liu, Q., Huang, C., & Wen, J. (2023). Study on performance and mechanisms of a novel integrated model with power & thermal management system and turbofan engine. Applied Thermal Engineering, 219, Article 119481. https://doi.org/10.1016/j.applthermaleng.2022.119481

[6] Zhu, Y., & Xuan, Y. (2026). A comprehensive model for energy management of adaptive cycle engine with integrating thermal inertia and variable mass effects. Aerospace Science and Technology, 168, Article 111109. https://doi.org/10.1016/j.ast.2025.111109

[7] Zhang, Y., Zou, Z., Fu, C., Wang, Y., & Zeng, J. (2026). Aerothermal performance of turbine during flight cycle based on fluid-thermal-structure multidisciplinary coupling method. Chinese Journal of Aeronautics, 39(1), Article 103691. https://doi.org/10.1016/j.cja.2025.103691

[8] Chapman, J. W., Lavelle, T. M., & Litt, J. S. (2016). Practical techniques for modeling gas turbine engine performance (NASA/TM-2016-219147). National Aeronautics and Space Administration. https://ntrs.nasa.gov/citations/20160012485

[9] Hendricks, E. S., & Gray, J. S. (2019). pyCycle: A tool for efficient optimization of gas turbine engine cycles. Aerospace, 6(8), Article 87. https://doi.org/10.3390/aerospace6080087

[10] Becker, R.-G., Wolters, F., Nauroz, M., & Otten, T. (2011, September 27-29). Development of a gas turbine performance code and its application to preliminary engine design [Conference paper, Paper 241485]. Deutscher Luft- und Raumfahrtkongress, Bremen, Germany. https://elib.dlr.de/73232/

[11] Greitzer, E. M. (1976). Surge and rotating stall in axial flow compressors—Part I: Theoretical compression system model. Journal of Engineering for Power, 98(2), 190-198. https://doi.org/10.1115/1.3446138

[12] Padture, N. P., Gell, M., & Jordan, E. H. (2002). Thermal barrier coatings for gas-turbine engine applications. Science, 296(5566), 280-284. https://doi.org/10.1126/science.1068609

[13] Evans, A. G., Mumm, D. R., Hutchinson, J. W., Meier, G. H., & Pettit, F. S. (2001). Mechanisms controlling the durability of thermal barrier coatings. Progress in Materials Science, 46(5), 505-553. https://doi.org/10.1016/S0079-6425(00)00020-7

[14] Schlichting, K. W., Padture, N. P., Jordan, E. H., & Gell, M. (2003). Failure modes in plasma-sprayed thermal barrier coatings. Materials Science and Engineering: A, 342(1-2), 120-130. https://doi.org/10.1016/S0921-5093(02)00251-4

[15] Nelson, H. D., & McVaugh, J. M. (1976). The dynamics of rotor-bearing systems using finite elements. Journal of Engineering for Industry, 98(2), 593-600. https://doi.org/10.1115/1.3438942

[16] Maslen, E. H., & Schweitzer, G. (Eds.). (2009). Magnetic bearings: Theory, design, and application to rotating machinery. Springer. https://doi.org/10.1007/978-3-642-00497-1

[17] Xu, B., Zhou, J., & Xu, L. (2024). Vibration suppression for a slice rotor supported by active magnetic bearings based on fractional-order adaptive backstepping control. Mechanical Systems and Signal Processing, 210, Article 111160. https://doi.org/10.1016/j.ymssp.2024.111160

[18] Moharrami, A., Choudhury, T., Ranjan, G., Ghalamchi, B., Ebel, H., & Sopanen, J. (2025). A physics-based and data-driven framework providing a guideline for state estimation in active magnetic bearing-supported rotors. Mechanism and Machine Theory, 217, Article 106250. https://doi.org/10.1016/j.mechmachtheory.2025.106250

[19] Storn, R., & Price, K. (1997). Differential evolution - A simple and efficient heuristic for global optimization over continuous spaces. Journal of Global Optimization, 11(4), 341-359. https://doi.org/10.1023/A:1008202821328

[20] Reed, R. C. (2006). The superalloys: Fundamentals and applications. Cambridge University Press. https://doi.org/10.1017/CBO9780511541285

[21] Miner, M. A. (1945). Cumulative damage in fatigue. Journal of Applied Mechanics, 12(3), A159-A164. https://doi.org/10.1115/1.4009458

[22] Larson, F. R., & Miller, J. (1952). A time-temperature relationship for rupture and creep stresses. Transactions of the ASME, 74(5), 765-771. https://doi.org/10.1115/1.4015909

[23] May, R. D., Csank, J., Lavelle, T. M., Litt, J. S., & Guo, T.-H. (2010). A high-fidelity simulation of a generic commercial aircraft engine and controller (NASA/TM-2010-216810). National Aeronautics and Space Administration. https://ntrs.nasa.gov/citations/20100037767

[24] Guo, T.-H., Lavelle, T. M., Litt, J. S., Csank, J., & May, R. D. (2011). Commercial modular aero-propulsion system simulation 40k (NASA Tech Brief LEW-18624-1). National Aeronautics and Space Administration. https://ntrs.nasa.gov/citations/20120000466

[25] Wilson, E. B. (1927). Probable inference, the law of succession, and statistical inference. Journal of the American Statistical Association, 22(158), 209-212. https://doi.org/10.1080/01621459.1927.10502953

[26] Brown, L. D., Cai, T. T., & DasGupta, A. (2001). Interval estimation for a binomial proportion. Statistical Science, 16(2), 101-133. https://doi.org/10.1214/ss/1009213286

[27] Sobol′, I. M. (2001). Global sensitivity indices for nonlinear mathematical models and their Monte Carlo estimates. Mathematics and Computers in Simulation, 55(1-3), 271-280. https://doi.org/10.1016/S0378-4754(00)00270-6

Supplementary Files

This is a list of supplementary files associated with this preprint. Click to download.

- KAM40ROnlineResource1.zip